Size Dependent CO2 Reduction Activity of Ag Nanoparticle Electrocatalysts

Xingyi Deng (xingyi.deng@netl.doe.gov)
National Energy Technology Laboratory https://orcid.org/0000-0001-9109-1443
Dominic Alfonso
National Energy Technology Laboratory
Thuy-Duong Nguyen-Phan
National Energy Technology Laboratory
Douglas Kauffman
National Energy Technology Laboratory https://orcid.org/0000-0002-7855-3428

Article

Keywords: electrocatalysis, CO2 reduction reaction, Ag catalysts

Posted Date: November 5th, 2021

DOI: https://doi.org/10.21203/rs.3.rs-1028834/v1

Size Dependent CO_2 Reduction Activity of Ag Nanoparticle Electrocatalysts

Xingyi Deng,[*,1,2] *Dominic Alfonso,*[*,1] *Thuy-Duong Nguyen-Phan,*[1,2] *and Douglas R. Kauffman*[*,1]

1. National Energy Technology Laboratory, 626 Cochrans Mill Road, P.O. Box 10940, Pittsburgh, PA 15236-0940, USA

2. NETL Support Contractor, 626 Cochrans Mill Road, P.O. Box 10940, Pittsburgh, PA 15236-0940, USA

***Email:** Xingyi.Deng@NETL.DOE.GOV; Dominic.Alfonso@NETL.DOE.GOV; Douglas.Kauffman@NETL.DOE.GOV

Abstract.

Coinage metals (Au, Cu and Ag) are state-of-the-art electrocatalysts for the CO_2 reduction reaction (CO_2RR). Size-dependent CO_2RR activity of Au and Cu has been studied, and increased H_2 evolution reaction (HER) activity is expected for small catalyst particles with high population of undercoordinated corner sites. A similar consensus is still lacking for Ag catalysts because the ligands and stabilizers typically used to control particle synthesis can block specific active sites and mask inherent structure-property trends. This knowledge gap is problematic because increased performance and catalyst utilization are still needed to improve economic viability. We combined density functional theory, microkinetic modeling, and experiment to demonstrate a strong size-dependence for pristine Ag particles in the sub-10 nm range. Small diameter particles with a high population of Ag edge sites were predicted to favor HER, whereas CO_2RR selectivity increased towards that of bulk Ag for larger diameter particles as the population of Ag(100) surface sites grew. Experimental results validated these predictions and we identified an optimal particle diameter of 8-10 nm that balanced selectivity and activity. Particles below this diameter suffered from poor selectivity, while larger particles demonstrated bulk-like activity and reduced catalyst utilization. These results demonstrate the size-dependent CO_2RR activity of pristine Ag catalysts and will help guide future development efforts.

Introduction.

The electrochemical CO_2 reduction reaction (CO_2RR) is a leading candidate for producing sustainable chemicals and fuels from waste carbon emissions.[1,2] Carbon monoxide (CO) is an appealing product because it is a versatile chemical building block, it only requires two electrons per molecule, and it can be formed with high-current density and Faradaic efficiency (FE).[3] The H_2 evolution reaction (HER) can also occur at CO_2RR-relevant electrochemical potentials, and competition between the two reactions can reduce product selectivity and energy efficiency. Precious-metal free catalysts have demonstrated promising CO_2RR activity and CO selectivity,[4-9] but gold and silver are still state-of-the-art materials for selective CO production.[10-14] A key challenge for deploying economically-viable electrochemical systems is reducing precious metal requirements by maximizing catalyst utilization.

Optimizing nanoparticle size is one approach to maximize catalyst usage and reduce total metal loading. Size-dependent CO_2RR vs. HER is well understood at Au and Cu nanoparticles thanks to agreement between experimental and theoretical investigations,[15-18] and it is generally agreed that a higher density of undercoordinated corner sites on smaller diameter nanoparticles can increase H_2 production and reduce selectivity toward CO. However, there is still a lack of fundamental consensus on how size-dependent CO selectivity and activity evolve for pristine Ag nanoparticles because the ligands, capping agents, and/or stabilizers often used to control nanoparticle size, shape, and crystallographic orientation can block, passivate, or modify specific surface sites.[19-24] This poses a challenge for optimizing Ag electrocatalysts because understanding the inherent CO_2RR *vs.* HER selectivity is needed to develop higher activity catalysts and reduce metal usage.

Ag nanocatalysts generally produce higher geometric current densities than bulk Ag particles and polycrystalline Ag foils,[11,21-29] but the use of various synthetic techniques has made it difficult

to identify consistent structure-property relationships. For example, the increased performance of oxide-derived[26-28] and AgCl-derived[29] Ag nanocatalysts has been attributed to increased surface area, enhanced intermediate stabilization, unique surface defects, preferential crystallographic orientations, and/or the presence of residual chloride ions. Size-dependent CO_2RR performance of cysteamine-capped Ag nanoparticles was attributed to sulfur atoms at the catalyst-ligand interface modifying intermediate bonding.[22,23] The performance of citrate-stabilized Ag nanoplates[21] and nanoprisms[24] was attributed to preferential expression of specific crystallographic faces and formation of stacked "super structures," but the identification of different active sites in nanoplates *vs.* nanoprisms and the role of citrate capping agents leave unresolved questions. Finally, previous calculations have also predicted that Ag particles as small as 2 nm may still retain high CO_2RR selectivity.[30] The above noted examples indicate that size, surface structure, and crystallographic orientation can all impact the CO_2RR activity of Ag nanocatalysts, but a clear understanding of the inherent, size-dependent activity of pristine Ag catalysts is still lacking in the literature.

Here, we used a combination of density functional theory (DFT), kinetic rate theory calculations, and microkinetic modeling (MKM) to predict the size-dependent CO_2RR performance of pristine Ag nanocatalysts. DFT and MKM calculations determined that CO_2RR and HER activity were dominated by electrochemically-accessible Ag(100) sites and Ag edge sites, respectively. These results were then combined with Ag nanoparticle Wulff constructions[21,22,31,32] to predict size-dependent CO_2RR and HER reactivity trends, showing increased CO_2RR selectivity with nanoparticle diameter as the population of Ag(100) sites increased and the population of Ag edge sites decreased. Interestingly, it was the Ag edge sites that impacted HER, whereas undercoordinated corner sites are believed to most strongly impact HER from Au and Cu nanoparticles.[15-18]

Finally, we directly validated our computational results by preparing and evaluating the CO_2RR performance of a series of pristine Ag nanocatalysts with well-controlled diameters. Experimental data revealed increased CO_2RR selectivity and activity with increasing particle diameter, and we identified Ag particles in the 8-10 nm range as the optimum balance of selectivity and catalyst usage on a total atom basis. Our results showed that pristine Ag catalysts demonstrate similar size-dependent CO_2RR selectivity trends as other coinage metals, albeit with unique CO_2RR *vs.* HER active sites, and fill a current gap in the literature that is needed to maximize the performance of Ag-based CO_2RR catalysts. This information provides new insight into a state-of-the-art CO_2RR catalyst and will help guide future materials design and optimization efforts.

Results and Discussion

We used Wulff constructions to analyze the size-dependent surface structure of Ag nanoparticles with diameters between 0.8-9.8 nm (**Figure 1a**).[21,22,31,32] The resulting nanoparticle structures were based on the DFT-calculated surface energies of the two low-index Ag(111) and Ag(100) facets, and the relative fraction of (100), (111), edge, and corner sites were extracted for each particle diameter. **Figure 1b** presents the total atomic population *vs*. nanoparticle diameter, showing the number of electrochemically-inaccessible bulk (interior) atoms rapidly increased with nanoparticle diameter. **Figure 1c** summarizes the relative population of electrochemically-accessible surface sites, excluding the interior bulk atoms. This presentation clearly shows the fraction of accessible corner and edge sites quickly decreased with particle diameter, while the fraction of accessible Ag(111) and Ag(100) sites increased with particle diameter.

DFT, rate theory calculations, and MKM were used to predict site-specific CO_2RR and HER rates at an experimentally-relevant potential of -1.0 V *vs.* the standard hydrogen electrode (SHE).

Similar methodology was previously used to predict CO_2RR kinetic barriers at Cu surfaces,[33,34] and specific computational details are provided in Supplementary Information. We considered CO and H_2 formation through the following elementary steps, where * represents a vacant active site or bound intermediate:

(i) $CO_2 + e^- + H^+ + * \rightarrow *COOH$

(ii) $*COOH + e^- + H^+ \rightarrow *CO + H_2O$

(iii) $*CO \rightarrow CO + *$

(iv) $H^+ + e^- + * \rightarrow *H$

(v) $*H + *H \rightarrow H_2 + *$

We employed a method to determine the potential-dependent reaction barrier ($\Delta G^{\#}$) of an electrochemical reduction via Bronsted-Evans-Polanyi extrapolation of the transition state barrier of an analogous non-electrochemical hydrogenation step.[35] The elementary step with the largest reaction barrier ($\Delta G^{\#}_{max}$) was considered to be the rate limiting step that established the forward rate constant (k_f) *via* $k_f = \frac{k_B T}{h} exp\left(-\frac{\Delta G^{\#}_{max}}{k_B T}\right)$.[36] The resulting k_f values were then incorporated into our MKM to predict product formation rates (r = molecules/atom$_{Ag}$/s) based on local concentration of reactants at the catalyst surface. This approach provides additional kinetic insight compared with exclusively using the computational hydrogen electrode (CHE) methodology to identify thermodynamically-challenging, potential-limiting reaction steps based Gibbs free energy changes.[37,38] In particular, rate determining and potential limiting steps may differ once transition state barriers are considered.

Relative CO_2RR and HER rates at an applied electrochemical potential of -1V *vs.* SHE were calculated for each site (**Figure S1**), and Ag(100) was predicted to be the most CO_2RR active site.

Figure 2a and **Table S1** show Ag(100) demonstrated the smallest $\Delta G^{\#}_{\max\,(CO2RR)}$ and largest $k_{f\,(CO2RR)}$ among the sites considered, and we identified the proton-coupled electron transfer to CO_2 that results in O-H bond formation to form *COOH (step i) as the rate limiting CO_2RR step. The corresponding transition state involved a water assisted H-shuttling model as shown in **Figure 2b**. The adsorbed $*CO_2$ was significantly bent relative to its linear gaseous counterpart, with a ~130° O-C-O bond angle and a Bader charge of -0.89*e* that resembled an adsorbed $*CO_2^{\delta-}$ species.[36] This adsorbed $*CO_2^{\delta-}$ species was hydrogen bonded to a nearby $H_3O^{\delta+}$-like species (a Bader charge of +0.77*e* summed over H_3O). Thus, a structure resembling a $CO_2^{\delta-}$– $H_3O^{\delta+}$ pair is seen in the transition state with net Bader charge of -0.12*e* that indicated partial reduction.

*COOH formation was also the rate limiting elementary step for CO_2RR at Ag edge sites and the transition state involved a similar water assisted H-shuttling model (**Figure S2**). A bent $*CO_2^{\delta-}$ was also observed with O-C-O angle of 131° and Bader charge of -0.75*e*. Aside from this, the transition state character is markedly different from that on Ag(100) because it lacked a $CO_2^{\delta-}$–$H_3O^{\delta+}$ pair. Rather, $CO_2^{\delta-}$ weakly interacted with the nearby H_2O as evidenced by a long H(water) – O(CO_2) interatomic distance of 1.63 Å. This longer bond distanced reduced the stabilization of the $*CO_2^{\delta-}$ moiety and resulted in increased $\Delta G^{\#}_{\max\,(CO2RR)}$, lowered $k_{f\,(CO2RR)}$, and decreased predicted CO_2RR kinetics compared with Ag(100) sites.

Elementary step ii (*CO formation) was the rate limiting process for both Ag(111) and Ag corner sites (**Figure S2**). In this transition state configuration, the OH fragment has moved away from the *COOH moiety, with a hydrogen bond to a H of $*H_2O$. Furthermore, the surface H has moved towards the H_2O suggesting the shuttling of H is in progress. The larger $\Delta G^{\#}_{\max\,(CO2RR)}$

values associated with these transition states produced smaller $k_{f\,(CO2RR)}$ values and resulted in lower predicted CO_2RR rates compared with Ag(100) or Ag edge sites.

On the other hand, Ag edge sites were predicted to be the most HER active (**Figure S1**) with the lowest $\Delta G^{\#}_{max\,(HER)}$ and largest $k_{f\,(HER)}$ (**Figure 2a** and **Table S2**). Elementary step (v) was identified as the rate limiting HER step at all sites, but different transition state geometries impacted the relative HER rates. For example, **Figure 2c** shows a late transition state at the Ag edge site with the H_2 product essentially formed. Interaction between the undercoordinated Ag surface and the adsorbed H_2 moiety stabilized the transition state and created H-H bond distance of ~ 0.8 Å. In comparison, an interatomic H-H distance of ~0.74 Å is expected for the gaseous H_2 product. Conversely, the this nearly-formed H_2 moiety is absent at other sites (**Figure S3**), and the transition states more closely resembled separate one-fold coordinated, weakly interacting *H species with H-H interatomic distances between ~1.2 – 1.6 Å. These separately adsorbed *H species created less stable transition states that increased $\Delta G^{\#}_{max\,(HER)}$, reduced $k_{f\,(HER)}$, and lowered HER rates compared with the transition state associated with the Ag edge site.

While our MKM considered the surface concentration of reactant molecules to calculate overall reaction rates, analysis of $\Delta G^{\#}_{max}$ and k_f values is instructive because it shows that Ag(100) sites and Ag edge sites were the most inherently CO_2RR and HER active sites, respectively. Notably, corner site atoms did not display the highest HER rates, which differs from the expected HER activity of under-coordinated corner sites at Au[15] and Cu[16] nanoparticles. We also note that CHE calculations identified elementary steps i (*COOH formation) and iv (*H formation) as the most thermodynamically challenging steps (*i.e.* the potential limiting steps) for CO_2RR and HER at all sites when only considering Gibbs free energy changes (**Figure S4**).[30] The discrepancy between thermodynamically-determined potential limiting steps and kinetically-determined rate

limiting steps highlights the importance of including transition state barriers to predict the relative CO_2RR and HER activity of catalyst sites.

We then predicted size-dependent CO_2RR and HER rates using the site-specific reaction rates and the population of each site as a function of nanoparticle diameter (**Figure 2d)**. Deconvoluting the size-dependent rate contributions revealed that CO_2RR and HER activity was dominated by Ag(100) and Ag edge sites, respectively (**Figure 2d and S5**). Electrochemically-accessible Ag(100) sites were responsible for 88-99% of the total CO_2RR rate for particle diameters above 2 nm. Rates initially increased with particle diameter as the population of Ag(100) sites became larger, but values decreased slightly above a diameter of 4 nm as the number of electrochemically-inaccessible bulk (interior) atoms became larger. This points to decreased catalyst utilization based on total metal content, but surface-normalized CO_2RR rates steadily increased with particle diameter when only considering electrochemically-accessible surface atoms (**Figure S6**). On the other hand, the Ag edge sites shown in **Figure 2c** contributed ~95-99% of the total HER activity at all particle sizes, and the relative HER rate decreased with particle diameter as the population of accessible Ag edge sites became smaller. These results predict that improved CO_2RR performance should be observed with increasing Ag nanoparticle diameter, but decreased catalyst utilization may occur above a critical catalyst size.

To validate these computational predictions, we created a series of pristine Ag nanoparticles with well-controlled diameters between 5-10 nm and evaluated their size-dependent electrocatalytic activity (details in Supplementary Information). Ag nanoparticles were prepared via e-beam evaporation onto a highly oriented pyrolytic graphite (HOPG) support in an ultra-high vacuum (UHV) chamber, providing a model system mimicking conventional carbon-supported Ag electrocatalysts. SEM images in **Figure 3a** show the average diameter grew from ~5 nm at a

loading of 0.7 $nmol_{Ag}/cm^2$ to ~10 nm at a loading of 4.4 $nmol_{Ag}/cm^2$. Particle diameters correlated well with Ag loading (**Figure S7**) and XPS confirmed all particles formed as metallic Ag (**Figure S8**). Our experimental approach eliminated the need for capping-agents, surfactants, or other surface-bound ligands typically used for size- or shape-controlled nanoparticle synthesis.[19-22] This allowed accurate comparison between theoretical and experimental results since organic ligands or other capping agents may block specific surface sites and/or modify the intrinsic catalytic properties.[22]

Samples were transferred from UHV and their electrocatalytic properties were evaluated in CO_2 saturated 0.1M $KHCO_3$ using an H-cell with a custom-built electrode holder (**Figure S9**). Contributions from catalyst-free regions of the HOPG surface were subtracted from the raw data (**Figure S10**), and CO and H_2 FEs were calculated from the detected products and HOPG-subtracted electrolysis charge (details in Supplementary Information). Potential-dependent CO_2RR experiments identified a maximum FE_{CO} at -1.2V *versus* the reversible hydrogen electrode (RHE) for both Ag nanoparticles and a bulk, polycrystalline Ag foil (**Figure S10c**), which is consistent with previous reports using single-crystal and polycrystalline Ag electrodes.[21,22,26,39] This cathodic potential was selected to evaluate the size-dependent electrocatalytic activity because it achieved the highest FE_{CO} and produced sufficient product for accurate CO and H_2 quantification at all loadings, and **Figure 3b** presents the FE_{CO} and FE_{H2} at -1.2V *vs.* RHE *versus* Ag particle diameter. The total FE for CO and H_2 production at -1.2V was close to 100% for samples with Ag loadings ≥ 1 $nmol_{Ag}/cm^2$ (**Table S2**), which validated our protocol for subtracting contributions from the HOPG substrate. The FE_{CO} increased with Ag diameter from ~20% FE_{CO} for ~5 nm diameter particles (<1.0 $nmol_{Ag}/cm^2$) to >90% FE_{CO} for particle diameters above 8 nm (>2.2 $nmol_{Ag}/cm^2$). Accordingly, FE_{H2} decreased from ~60% to < 5% FE_{H2} with increased particle

diameter. In comparison, a bulk Ag foil produced ~90% FE_{CO} at -1.2V (**Figure 3b**), which indicates Ag particles above ~8 nm diameter demonstrated "bulk-like" product selectivity. A similar trend size-dependent FE_{CO} trend was also observed at -1.0V and -1.1V *vs.* RHE (**Figure S11**), but the small current densities produced in this low loading regime made H_2 quantification difficult below -1.2V *vs.* RHE.

Figure 3c presents the size-dependent turnover frequency (TOF: molecules/$atom_{Ag}$/s) for CO and H_2 production estimated from the XPS-determined Ag loading (mol_{Ag}/cm^2) and the moles of CO or H_2 produced during the electroreduction experiments. TOF_{CO} gradually increased from 0.2 to ~1 CO/$atom_{Ag}$/s with increasing particle diameter, while TOF_{H2} decreased more than an order of magnitude from 0.9 to 0.02 H_2/$atom_{Ag}$/s. Interestingly, the nanoparticle TOF values converged with bulk Ag above a diameter of ~8 nm. Since the XPS probe depth was estimated to be ~1.6 nm based on the universal curve for the electron inelastic mean free path in elements (details in Supplementary Information),[40] the Ag loadings determined from XPS measurements included a substantial amount of electrochemically-inaccessible interior Ag atoms that did not participate in the reactions. The slow CO TOF increase and eventual convergence with bulk Ag is likely due to the growing population of electrochemically-inaccessible atoms included in the TOF calculations, while the quick H_2 decline was due to the rapid decrease in edge sites and the growing population of electrochemically-inaccessible interior atoms. The experimentally-measured TOFs are qualitatively consistent with the MKM simulated trends shown in **Figure 2d** and validate these computational predictions.

Finally, the convergence with bulk TOF values above ~8 nm diameter does not necessarily conflict with previous reports that observed increased geometric current density from nanostructured Ag catalysts.[11,21-29] Catalyst loadings in these previous studies were typically

several orders of magnitude higher than this study, and reported enhancements in current density from Ag nanocatalysts largely stemmed from a higher fraction of electrochemically-active surface area compared with bulk catalysts. In our low-loading regime (<4.5 nmol/cm^2) the Ag nanoparticles formed at low coverages and contained a smaller number Ag atoms than the bulk Ag foil (27.4 nmol/cm^2 based on XPS). This produced low geometric current densities (0.6-1.2 mA/cm^2), but it allowed us to accurately measure intrinsic activity differences and identify size-dependent trends. Our results show size-related effects are important in the sub-10 nm range and we identified an optimum particle size of 8-10 nm that balanced CO_2RR selectivity and catalyst utilization. Particles below this diameter suffered from reduced CO_2RR selectivity, whereas particle diameters above ~10 nm will experience low catalyst utilization on a total atom basis.

In conclusion, we have coupled DFT, rate theory calculations, microkinetic modeling, and experimental evaluations to identify the size-dependent CO_2RR activity of pristine Ag nanoparticles prepared without ligands, capping agents, or other stabilizers. Ag demonstrated a decrease in CO_2RR activity at smaller sizes that is similar to other Au and Cu coinage metal catalysts. However, the specific sites responsible for CO_2RR and HER were unique. We found that CO_2RR and HER activity was dominated by Ag(100) and Ag edge sites respectively, whereas corner sites did not contribute significantly to HER. Small Ag particles favored HER due to a higher population of Ag edge sites. CO_2RR selectivity increased with particle diameter as the relative population of Ag(100) sites grew, and the population of Ag edge sites decreased. Our experimental results also allowed us to identify 8-10 nm as the optimum Ag particle diameter to maximize both CO_2RR selectivity and catalyst usage. This information provides new insight into the inherent CO_2RR activity of Ag nanocatalysts and should be useful for future catalyst design.

Methods

Computational methods. Ag nanoparticle models were represented via the Wulff construction to quantify the density of active surface sites for a given cluster diameter.[31,32] The Wulff construction is based on the DFT calculated surface energies of the low-index Ag(100) and Ag(111) facets. Ag(111) and Ag(100) with 3 and 5 dangling bonds in each surface atom, respectively, represent the two low index facets. Surface energies are calculated by taking the energy of the symmetric surface slab and the same amount of Ag units in the bulk, divided by twice the surface area of the slab: $\gamma = \frac{E_S - nE_B}{2A}$, where E_s, E_B, and A refer to the total energy of a surface slab containing n Ag atoms, total energy of bulk per Ag atom and the base area of the surface slab. The fractions of (100), (111), edge, and corner sites were then extracted for each facet of the clusters versus the cluster diameter.

Structure relaxations and single point energies were calculated using the density functional theory (DFT) as implemented in the Vienna *Ab Initio* Simulation Package (VASP) commercial software.[41] Periodic Ag(111) and Ag(100) slab models were used to represent the active sites on the low-index plane of the metal catalyst. Edge sites were represented using the internal step edge of a Ag(211) surface, as has been done previously.[30] To represent the corner sites, an icosahedral 147 atom Ag cluster (Ag_{147}) enclosed in a periodic 30 Å × 30 Å × 30 Å box was utilized.[30] Rate theory calculations and MKM were then used to predict site-specific CO_2RR and HER rates. More details about the DFT calculations and microkinetic simulations are provided in Supplementary Information.

Catalyst Growth and Characterization. All HOPG supported Ag catalysts (Ag/HOPG) were grown in a commercial ultrahigh vacuum (UHV) chamber from Omicron Nanotechnology GmbH

with a base pressure of ~2 × 10^{-10} mbar). This UHV chamber includes an electron-beam assisted evaporator (Omicron EFM3T) for metal catalysts deposition, X-ray photoelectron spectroscopy (XPS), scanning tunneling microscopy (STM), and a fast entry lock (FEL) for sample transfer between UHV and atmosphere. The HOPG surface (SPI-1 grade, 10 × 10 × 1 mm^3, SPI Supplies) was prepared by cleaving the surface with adhesive tape in air and then reintroduced into the UHV chamber through the FEL. Prior to metal evaporations, the cleaved HOPG surface was gently sputtered with Ar^+ (500 V, 1 mA, P_{Ar} = 3 × 10^{-7} mbar) for 1 min followed by annealing at T = 700 K for 5 min to remove embedded Ar and create defects for metal nucleation.[42]

Ag was evaporated onto the Ar^+ sputtered HOPG surface at room temperature using the e-beam assisted evaporator (Omicron EFM3T). The Ag evaporation rate was roughly maintained at ~2 × 10^{-11} mol/cm^2/min with variable evaporation time to control the loading of Ag on the Ar^+ sputtered HOPG substrate, and the actual Ag loading was estimated from the atomic ratio of Ag to C (from the XPS measurements comparing the Ag 3d and C 1s peaks) multiplied by the carbon atomic density of the graphene/graphite surface (3.82 × 10^{15} atoms/cm^2). As a reference for HOPG supported Ag catalysts, a Ag foil (10 × 10 × 1 mm^3, Sigma-Aldrich, 99.99%) was cleaned in the UHV chamber by cycles of Ar^+ sputtering (1.5 keV, 10 mA, P_{Ar} = 1 × 10^{-6} mbar) at room temperature and annealing at T = 700 K for 15 min until no impurities such as O and C were detected by XPS.

XPS measurements were carried out at room temperature using a Mg Kα X-ray source (1253.6 eV, 300 W) and a hemispheric analyzer with a pass energy of 20 eV. All binding energies were calibrated using the C 1s peak at BE = 284.3 eV. The XPS probe depth for Ag was ~1.6 nm, estimated from the universal curve for the electron inelastic mean free path in elements based on

equation $\lambda = \frac{143}{E^2} + 0.054 \times \sqrt{E}$, where E is the kinetic energy of photoelectrons.[40] For Ag 3d photoelectrons, E = 1253.6 – 368 (BE) ≈ 885 eV.

Scanning electron microscopy (SEM) characterizations were conducted on a FEI Quanta 600F microscope operated at 20 kV equipped with an energy-dispersive X-ray (EDX) detector. SEM images were analyzed with the ImageJ software (version 1.52a) to estimate the average Ag particle diameters, and the minimum particle size in the ImageJ analysis was set to 1 nm^2 to avoid measuring pixelated noise.

Electrochemistry measurements. Electrochemical CO_2 reduction experiments were carried out in a gas-tight H-Cell. A custom-built, polytetrafluoroethylene (PTFE) electrode holder sealed the base of the catholyte chamber and allowed measurement of the HOPG-supported samples (Figure S9). The catholyte and anolyte chambers were filled with 0.1 M $KHCO_3$ (99.99%, Sigma-Aldrich) prepared with ultra-pure deionized water (18.3 MΩ; Barnstead EASYpure LF) and separated by a proton-exchange membrane (Nafion 117). A leak-free Ag/AgCl reference electrode (eDAQ, Inc.) was housed in the catholyte chamber and a platinum wire counter electrode was housed in the anolyte chamber. The catholyte was continuously purged with CO_2 (99.999%, Butler gas) at a flow rate of 20 mL/min (pH ~ 6.8) during the experiments and the solution was stirred with a magnetic stir bar at 200 rpm to help minimize bubble formation on the HOPG substrates.

CO_2 reduction measurements were conducted at ambient pressure and temperature using a Biologic SP-150 potentiostat. Electrochemical potentials were converted into the reversible hydrogen electrode (RHE) scale with corrections made for the uncompensated resistance (R_{uc}) at the 85% values using the instrument software (iR-correction). Chronoamperometric experiments were conducted for 20 min at each applied potential. The evolved gas products (CO and H_2) were

collected in a gas tight Tedlar sampling bag and quantified by PerkinElmer Clarus 600GC equipped with a ShinCarbon ST 80/100 Column (He carrier gas) and both flame ionization and thermal conductivity detectors. The GC was calibrated routinely using a calibration mixture of gases with known composition. Details of calculating Faradaic efficiencies of the Ag/HOPG catalysts for each product, including corrections made by subtracting the HOPG contributions, are described in Supplementary Information.

Data Availability

All data supporting the findings of this study are available within the article and its Supplementary Information file, or from the corresponding authors upon request.

References

1. Kibria MG*, et al.* Electrochemical CO_2 Reduction into Chemical Feedstocks: From Mechanistic Electrocatalysis Models to System Design. *Adv. Mater.* **31**, 1807166 (2019).

2. Nitopi S*, et al.* Progress and Perspectives of Electrochemical CO_2 Reduction on Copper in Aqueous Electrolyte. *Chem. Rev.* **119**, 7610-7672 (2019).

3. Gao F-Y, Bao R-C, Gao M-R, Yu S-H. Electrochemical CO_2-to-CO Conversion: Electrocatalysts, Electrolytes, and Electrolyzers. *J. Mater. Chem. A* **8**, 15458-15478 (2020).

4. Zheng T, Jiang K, Wang H. Recent Advances in Electrochemical CO_2-to-CO Conversion on Heterogeneous Catalysts. *Adv. Mater.* **30**, 1802066 (2018).

5. Yang H*, et al.* A Universal Ligand Mediated Method for Large Scale Synthesis of Transition Metal Single Atom Catalysts. *Nat. Commun.* **10**, 4585 (2019).

6. Zhu Y, Yang X, Peng C, Priest C, Mei Y, Wu G. Carbon-Supported Single-Atom Catalysts: Carbon-Supported Single Metal Site Catalysts for Electrochemical CO_2 Reduction to CO and Beyond. *Small* **17**, 2005148 (2021).

7. Jia C, Dastafkan K, Ren W, Yang W, Zhao C. Carbon-based Catalysts for Electrochemical CO_2 Reduction. *Sustainable Energy Fuels* **3**, 2890-8906 (2019).

8. Zhang H, Cheng W, Luan D, Lou XWD. Atomically Dispersed Reactive Centers for Electrocatalytic CO_2 Reduction and Water Splitting. *Angew. Chem. Int. Ed.* **60**, 13177-13196 (2021).

9. Wang Y*, et al.* Advanced Electrocatalysts with Single-Metal-Atom Active Sites. *Chem. Rev.* **120**, 12217-12314 (2020).

10. Kaczur JJ, Yang H, Liu Z, Sajjad SD, Masel RI. A Review of the Use of Immobilized Ionic Liquids in the Electrochemical Conversion of CO_2. *J. Carbon Research* **6**, 33 (2020).

11. Lu Q*, et al.* A Selective and Efficient Electrocatalyst for Carbon Dioxide Reduction. *Nat. Commun.* **5**, 3242 (2014).

12. An Overview on the Recent Developments of Ag-based Electrodes in the Electrochemical Reduction of CO_2 to CO. *Sustainable Energy Fuels* **4**, 50-67 (2020).

13. Zhu W*, et al.* Active and Selective Conversion of CO_2 to CO on Ultrathin Au Nanowires. *J. Am. Chem. Soc.* **136**, 16132-16135 (2014).

14. Zhu W*, et al.* Monodisperse Au Nanoparticles for Selective Electrocatalytic Reduction of CO_2 to CO. *J. Am. Chem. Soc.* **135**, 16833-16836 (2013).

15. Mistry H*, et al.* Exceptional Size-Dependent Activity Enhancement in the Electroreduction of CO_2 over Au Nanoparticles. *J. Am. Chem. Soc.* **136**, 16473-16476 (2014).

16. Reske R, Mistry H, Behafarid F, Cuenya BR, Strasser P. Particle Size Effects in the Catalytic Electroreduction of CO_2 on Cu Nanoparticles. *J. Am. Chem. Soc.* **136**, 6978−6986 (2014).

17. Vickers JW, Alfonso D, Kauffman DR. Electrochemical Carbon Dioxide Reduction at Nanostructured Gold, Copper, and Alloy Materials. *Energy Technol.* **5**, 775-795 (2017).

18. Rong W*, et al.* Size-Dependent Activity and Selectivity of Atomic-LevelCopperNanoclustersduring CO/CO_2 Electroreduction. *Angew. Chem. Int. Ed.* **60**, 466-472 (2021).

19. Xia Y, Xiong Y, Lim B, Skrabalak SE. Shape-Controlled Synthesis of Metal Nanocrystals: Simple Chemistry Meets Complex Physics? *Angew. Chem. Int. Ed.* **48**, 60-103 (2008).

20. Xia X, Zeng J, Zhang Q, Moran CH, Xia Y. Recent Developments in Shape-Controlled Synthesis of Silver Nanocrystals. *J. Phys. Chem. C* **116**, 21647-21656 (2012).

21. Liu S*, et al.* Shape-Dependent Electrocatalytic Reduction of CO2 to CO on Triangular Silver Nanoplates. *J. Am. Chem. Soc.* **139**, 2160-2163 (2017).

22. Kim C*, et al.* Achieving Selective and Efficient Electrocatalytic Activity for CO_2 Reduction Using Immobilized Silver Nanoparticles. *J. Am. Chem. Soc.* **137**, 13844-13850 (2015).

23. Wang Z*, et al.* Surface Ligand Promotion of Carbon Dioxide Reduction through Stabilizing Chemisorbed Reactive Intermediates. *J. Phys. Chem. Lett.* **9**, 3057-3061 (2018).

24. Qi K*, et al.* Enhancing the CO_2-to-CO Conversion from 2D Silver Nanoprisms via Superstructure Assembly. *ACS Nano* **15**, 7682-7693 (2021).

25. Salehi-Khojin A*, et al.* Nanoparticle Silver Catalysts That Show Enhanced Activity for Carbon Dioxide Electrolysis. *J. Phys. Chem. C* **117**, 1627-1632 (2012).

26. Ma M, Trześniewski BJ, Xie J, Smith WA. Selective and Efficient Reduction of Carbon Dioxide to Carbon Monoxide on Oxide-Derived Nanostructured Silver Electrocatalysts. *Angew. Chem. Int. Ed.* **55**, 9748-9752 (2016).

27. Mistry H*, et al.* Enhanced Carbon Dioxide Electroreduction to Carbon Monoxide over Defect-Rich Plasma-Activated Silver Catalysts. *Angew. Chem. Int. Ed.* **56**, 11394-11398 (2017).

28. Peng X, Karakalos SG, Mustain WE. Preferentially Oriented Ag Nanocrystals with Extremely High Activity and Faradaic Efficiency for CO_2 Electrochemical Reduction to CO. *ACS Appl. Mater. Interfaces* **10**, 1734-1742 (2018).

29. Hsieh Y-C, Senanayake SD, Zhang Y, Xu W, Polyansky DE. Effect of Chloride Anions on the Synthesis and Enhanced Catalytic Activity of Silver Nanocoral Electrodes for CO_2 Electroreduction. *ACS Appl. Mater. Interfaces* **5**, 5349-5365 (2015).

30. Back S, Yeom MS, Jung Y. Active Sites of Au and Ag Nanoparticle Catalysts for CO_2 Electroreduction to CO. *ACS Catal.* **5**, 5089-5096 (2015).

31. Barmparis GD, Lodziana Z, Lopez N, Remediakis IN. Nanoparticle shapes by using Wulff constructions and first-principles calculations. *Beilstein J. Nanotechnol.* **6**, 361-368 (2015).

32. Wulff G. On the question of speed of growth and dissolution of crystal surfaces. *Z. Kristallogr.* **34**, 449 (1901).

33. Nie X, Luo W, Janik MJ, AravindAsthagiri. Reaction Mechanisms of CO_2 Electrochemical Reduction on Cu(1 1 1) Determined with Density Functional Theory. *J. Catal.* **312**, 108-122 (2014).

34. Nie X, Esopi MR, Janik MJ, Asthagiri A. Selectivity of CO_2 Reduction on Copper Electrodes: The Role of the Kinetics of Elementary Steps. *Angew. Chem. Int. Ed.* **52**, 2459-2462 (2013).

35. Clayborne A, Chun H-J, Rankin RB, Greeley J. Elucidation of Pathways for NO Electroreduction on Pt(111) from First Principles. *Angew. Chem. Int. Ed.* **54**, 8255-8258 (2015).

36. Singh MR, Goodpaster JD, Weber AZ, Head-Gordon M, Bell AT. Mechanistic Insights into Electrochemical Reduction of CO_2 over Ag Using Density Functional Theory and Transport Models. *Proc. Natl. Acad. Sci. USA* **114**, E8812-E8821 (2017).

37. Nørskov JK*, et al.* Origin of the Overpotential for Oxygen Reduction at a Fuel-Cell Cathode. *J. Phys. Chem. B* **108**, 17886-17892 (2004).

38. Calle-Vallejo F, Koper MTM. First-Principles Computational Electrochemistry: Achievements and Challenges. *Electrochim. Acta* **84**, 3-11 (2012).

39. Clark EL*, et al.* Influence of Atomic Surface Structure on the Activity of Ag for the Electrochemical Reduction of CO_2 to CO. *ACS Catal.* **9**, 4006-4014 (2019).

40. Seah MP, Dench WA. Quantitative Electron Spectroscopy of Surfaces: A Standard Data Base for Electron Inelastic Mean Free Paths in Solids. *Surf. Interface Anal.* **1**, 2-11 (1979).

41. Kresse G, Furthmüller J. Effeciency of Ab-Initio Total Energy Calculations for Metals and Semiconductors Using a Plane-Wave Basis Set *Comp. Mat. Sci.* **6**, 15-50 (1996).

42. Galhenage RP*, et al.* Platinum–Ruthenium Bimetallic Clusters on Graphite: a Comparison of Vapor Deposition and electroless Deposition Methods. *Phys. Chem. Chem. Phys.* **17**, 28354-28363 (2015).

Acknowledgements

This project was funded by the United States Department of Energy, National Energy Technology Laboratory, in part, through a site support contract. Neither the United States Government nor any agency thereof, nor any of their employees, nor the support contractor, nor any of their employees, makes any warranty, express or implied, or assumes any legal liability or responsibility for the accuracy, completeness, or usefulness of any information, apparatus, product, or process disclosed, or represents that its use would not infringe privately owned rights. Reference herein to any specific commercial product, process, or service by trade name, trademark, manufacturer, or otherwise does not necessarily constitute or imply its endorsement, recommendation, or favoring by the United States Government or any agency thereof. The views and opinions of authors expressed herein do not necessarily state or reflect those of the United States Government or any agency thereof.

Author Contributions

X.D., D.A. and D.R.K. supervised the project and co-wrote the paper. X.D. performed experiments, collected, and analyzed the experimental data. D.A carried out all theoretical calculations, including Wulff construction, DFT and microkinetic simulations. T.D.N.P. helped collect all SEM images. All authors discussed the results and commented on the paper.

Competing Interests

The authors declare no competing interests.

Additional Information

Supplementary Information available.

Correspondence and requests for materials should be addressed to Xingyi Deng, Dominic Alfonso, or Douglas R. Kauffman.

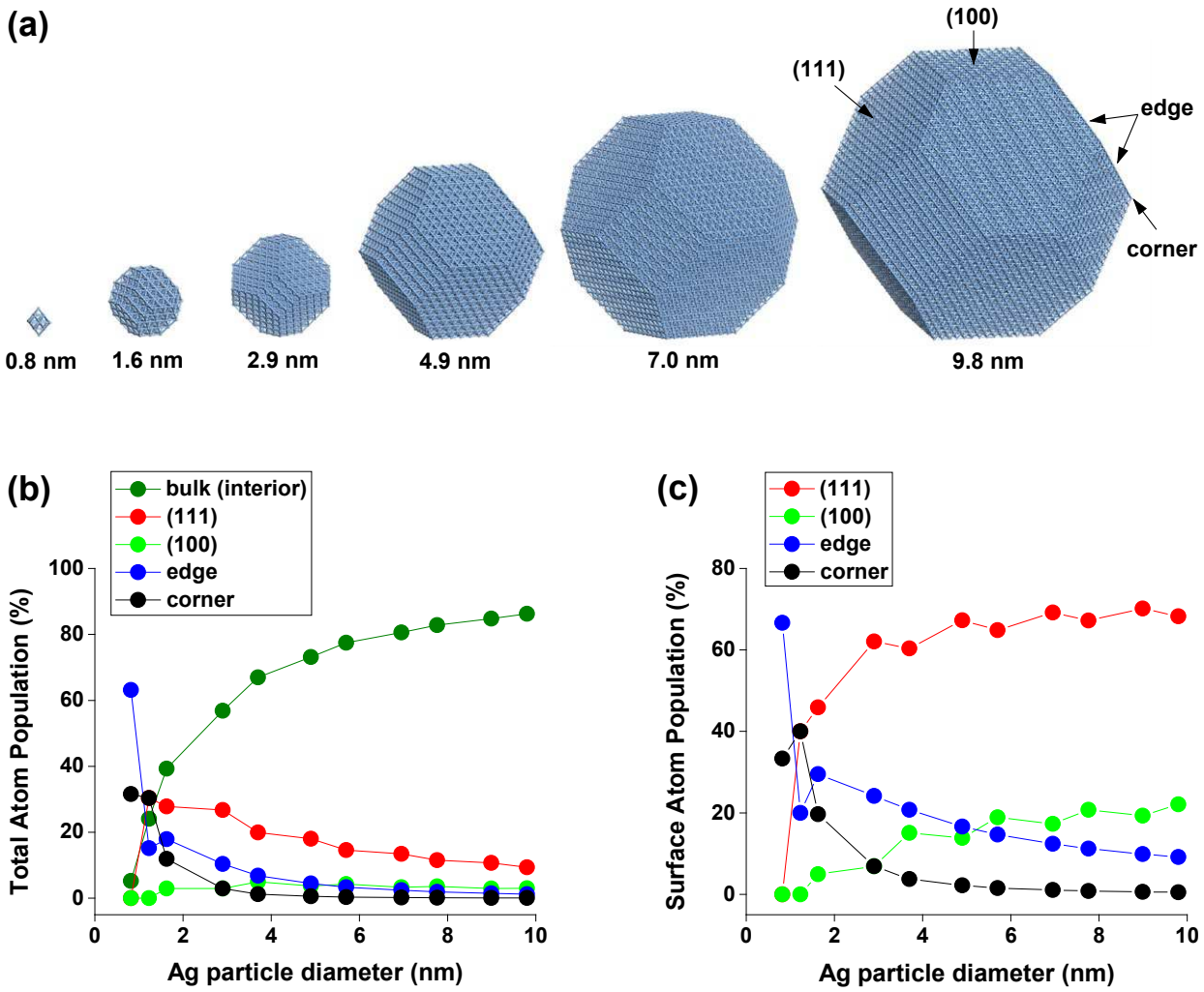

Figure 1. (a) Evolution of particle size/structure with size based on the Wulff construction. (b) Total atomic population of each site. (c) Population of surface atoms excluding electrochemically-inaccessible bulk (interior) atoms.

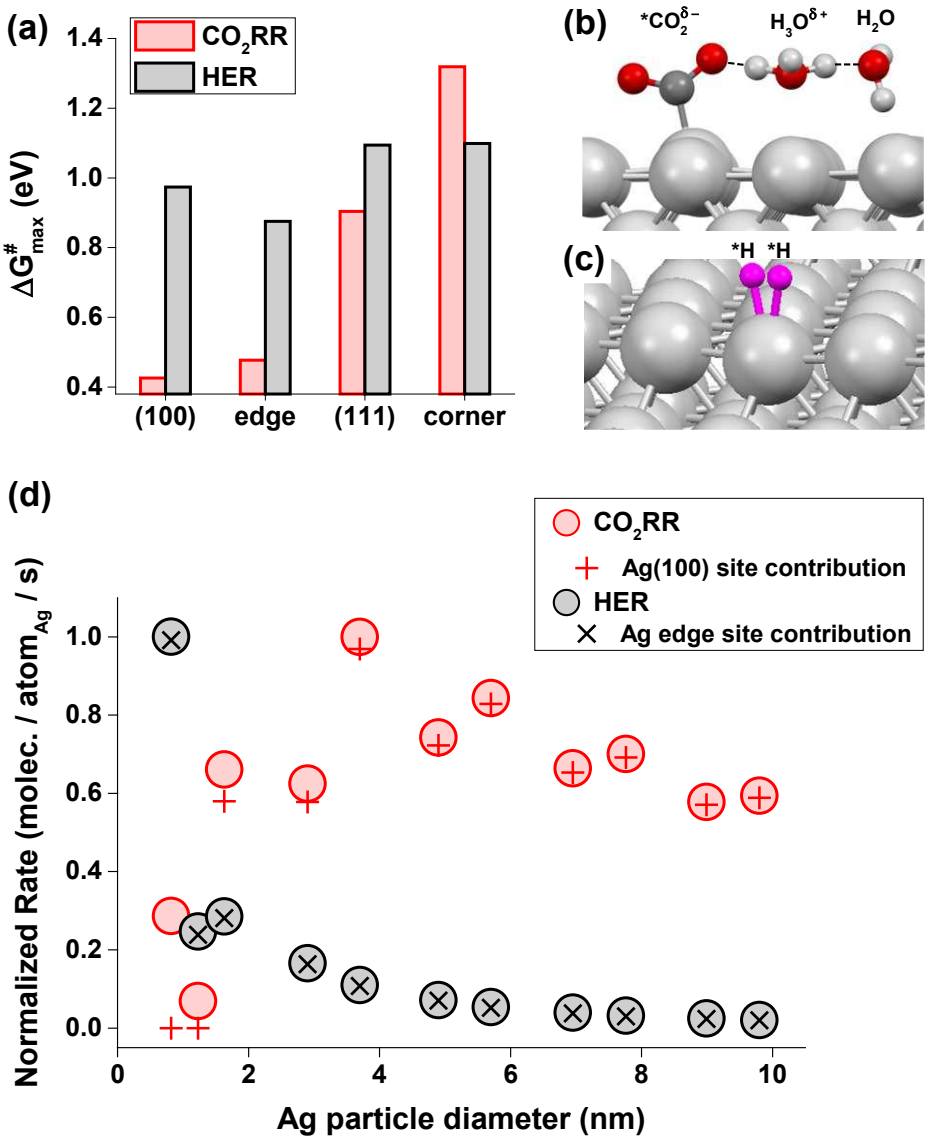

Figure 2. (a) Maximum CO_2RR and HER reaction barriers ($\Delta G^{\#}_{max}$) associated with the rate-determining steps at specific reaction sites. Transition state geometries for (b) CO_2RR at Ag (100) sites and (c) HER and Ag edge sites. (d) Size-depended CO_2RR and HER rates with the deconvoluted contribution of Ag(100) and Ag edge sites shown.

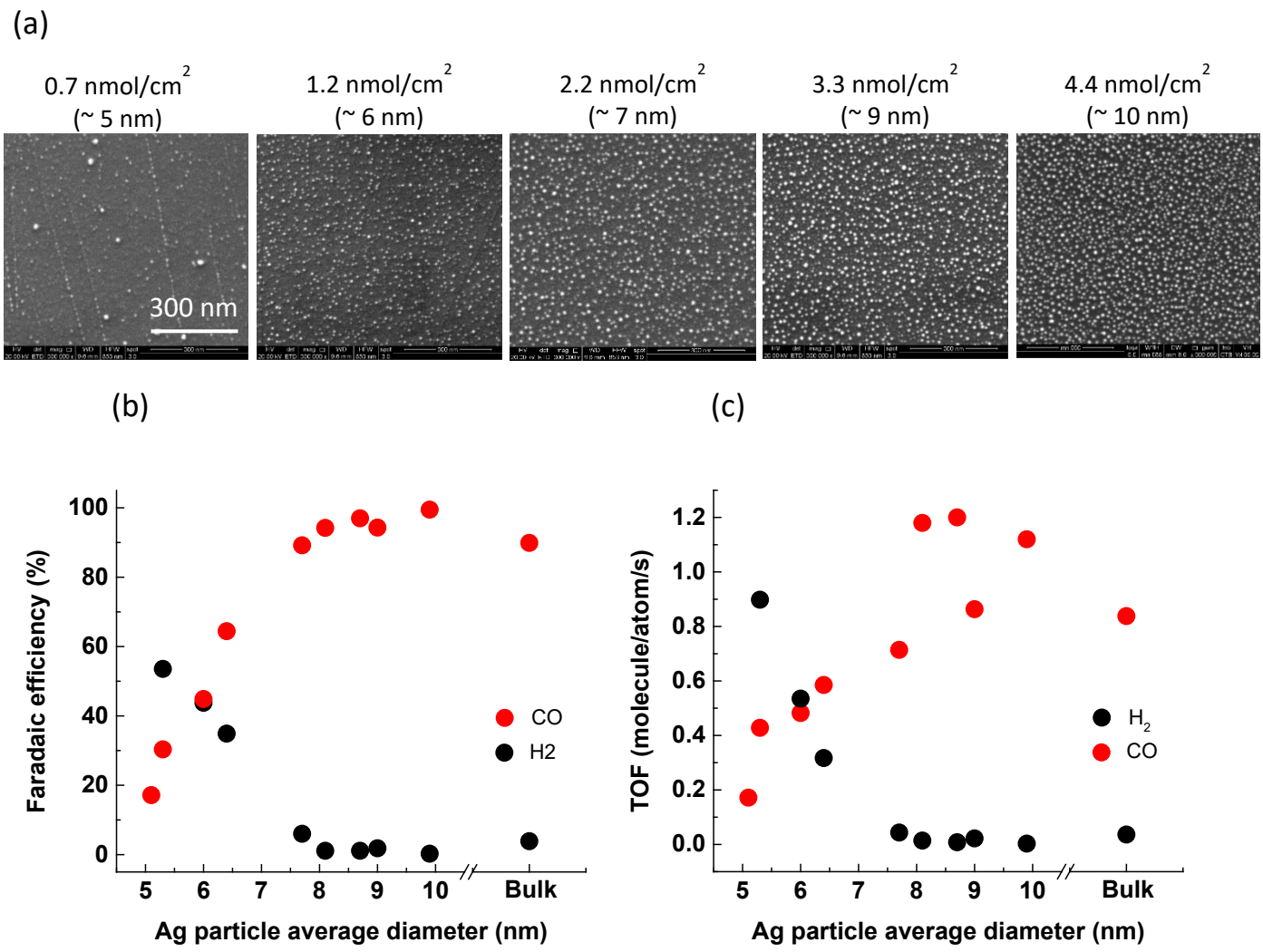

Figure 3. (a) Scanning electron microscopy (SEM) images of Ag/HOPG catalysts prepared via e-beam assisted evaporation in an ultrahigh vacuum (UHV) chamber, showing increasing particle size with Ag loading; scale bar is 300 nm. Ag particle size dependent (b) FE_{H2} and FE_{CO}, and (c) TOF_{H2} and TOF_{CO} of the Ag/HOPG catalysts and bulk Ag foil at -1.2 V vs. RHE in CO_2 saturated 0.1 M $KHCO_3$. For a sample with extremely small Ag loading (< 1 $nmol_{Ag}/cm^2$, ~ 5 nm particle size), H_2 was not quantified due to the instrument detection limit; however, CO FE and TOF still followed the trend.

Supplementary Files

This is a list of supplementary files associated with this preprint. Click to download.

- AgsizedependentCO2RRSINatComm.pdf